


Accurate and noise robust crosstalk removal techniques for edge illumination phase-based x-ray imaging systems

ANDREA MAZZOLANI,^{1,*}  ALBERTO ASTOLFO,¹ IAN BUCHANAN,¹ SAVVAS SAVVIDIS,¹ MARIUS DIDZIOKAS,² MEHRAN MOAZEN,¹ LUCA FARDIN,¹  PETER R. T. MUNRO,¹  AND ALESSANDRO OLIVO¹ 

¹Department of Medical Physics and Biomedical Engineering, University College London, Malet Place, Gower Street, London WC1E 6BT, UK

²Department of Mechanical Engineering, University College London, Roberts Engineering Building, Torrington Place, London WC1E 7JE, UK

*andrea.mazzolani.18@ucl.ac.uk

Abstract: In x-ray phase contrast imaging (XPCI) using the edge illumination method (EI), crosstalk (XT) between adjacent pixels due to, e.g., light diffusion in the scintillator in indirect conversion detector systems is an issue that blurs images and reduces both image sharpness and quantitative accuracy. We provide a detailed mathematical description of this phenomenon and propose two independent methods to mitigate its negative effects. The effectiveness of these techniques is demonstrated through both simulated and experimental data, showcasing the improvements in image quality and quantitative accuracy. In particular, the experimental data include an intact mouse skull where soft tissue details of the brain are visualized and improved with the proposed deconvolution methods; to the best of our knowledge, details of the murine brain structure inside an intact skull had not been observed before with laboratory-based XPCI systems.

Published by Optica Publishing Group under the terms of the [Creative Commons Attribution 4.0 License](https://creativecommons.org/licenses/by/4.0/). Further distribution of this work must maintain attribution to the author(s) and the published article's title, journal citation, and DOI.

1. Introduction

X-ray phase contrast imaging (XPCI) is a technique that enhances the visibility of details in x-ray images by utilizing the phase shifts that occur as x-rays pass through an object, rather than conventional attenuation-based mechanisms. This shift enhances image visibility, revealing details traditionally considered invisible to attenuation-based imaging. The superior sensitivity of XPCI stems from refractive effects, which are driven by a physical parameter (the unit decrement of the real part of the refractive index δ) approximately three orders of magnitude larger than that responsible for attenuation (the refractive index imaginary part β). This is particularly advantageous in distinguishing objects with similar attenuation coefficients [1], and in fact XPCI has demonstrated its potential in fields ranging from medical imaging [2–6] to material science [7], biology [8], and beyond.

Edge illumination (EI) is an XPCI technique originally developed in the late 1990s, at the Elettra Light Source in Trieste, Italy [9]. EI systems employ a dual-mask configuration: a sample mask (M_1) positioned upstream of the sample subdivides the x-ray beam into multiple individual beamlets, and a detector mask (M_2), aligned with the detector pixels and creating insensitive regions between them, analyses changes in the beamlets (especially their direction) caused by the interaction with the sample.

In EI systems, the M_2 apertures are positioned to illuminate the center of the pixels while obscuring the edges.

Like most x-ray imaging techniques, EI is affected by pixel crosstalk (XT), i.e., signal spillover into adjacent pixels caused by, e.g., light diffusion in the scintillator in indirect conversion detectors and charge sharing in direct conversion ones. This causes a smoothing of the refraction peaks in raw images, that affects the quantitiveness of subsequent phase retrieval procedures. The effect of XT can be mitigated by using skipped-mask apertures, in which case the apertures of both M_1 and M_2 illuminate every other pixel [10,11]. However, some degree of leftover XT is often still observed also in this case. Deconvolution methods can be used to reduce this residual XT. For example, Olivo and Speller [12] employed a deconvolution algorithm with Wiener filter to remove XT from images obtained with a different XPCI method, called free-space propagation [13], thereby sharpening the phase signal and enhancing spatial resolution, albeit at the cost of increased overall image noise. Havariyoun *et al.* [11] studied the effect of XT on the Modulation transfer Function of EI systems when skipped and non-skipped mask are employed. Ignatyev *et al.* [14] showed that the skipped mask EI architecture reduced XT from ~49% to ~6% with a 50 μm pixel indirect conversion flat panel detector, and assumed the latter to be a negligible amount of XT. They also demonstrated that, when a resolution-enhancement method termed "dithering" is employed, where multiple frames are acquired and combined while the sample is laterally moved in sub-pixel steps, XT is responsible for creating secondary fringe-like artifacts in the resulting images.

In this paper, we show mathematically how skipped-mask architecture EI systems are affected by XT, resulting in a reduction in spatial resolution, edge-doubling effects, and blurring. To address this, we propose two variants of a Fourier-based deconvolution algorithm: the first employs a high-frequency filter, while the second is based on circulant matrices. Notably, the second approach enhances image quality without introducing any noticeable increase in image noise. Our analysis is supported by testing the deconvolution models on both simulated and experimental data, clearly demonstrating improvements in image quality without negative effects from the typical noise amplification issues associated with deconvolution algorithms.

2. EI projections and retrieval

In EI systems, a bell-shaped curve referred to as "illumination curve" is obtained by scanning one mask (typically M_1) while the other is kept still; this is usually approximated with a Gaussian function, and we will represent it as a function of the variable t . We will also denote the analyzed detector row of pixels as x . The raw intensities measured at the detector, for all points on the acquired illumination curve, will be referred to as raw projections.

In particular, a raw projection as a function of t and x can be represented as a Gaussian function with an offset [15,16]:

$$P_F^0(x, t) = A_F(x)e^{-\frac{(t-B_F(x))^2}{2C_F(x)^2}} + D_F(x) \quad (1a)$$

$$P_S^0(x, t) = A_S(x)e^{-\frac{(t-B_S(x))^2}{2C_S(x)^2}} + D_S(x) \quad (1b)$$

where subscripts ' F ' and ' S ' refer to objects related to the projections without and with sample, respectively, P^0 represents the raw projection, $A(x)$ and $C(x)$ are used to calculate the attenuation, $B(x)$ accounts for the shift of the illumination curve caused by sample refraction, the standard deviation $C(x)$ is used to estimate the scattering within the illuminated sample, and $D(x)$ represents the offset of the Gaussian, encoding factors such as mask transmittance, long tails in the source distribution, scattering from air, etc. It is worth noting that Eqs. (1a) do not include the PSF; however, the Gaussian assumption remains valid by assuming an extended source having a Gaussian spatial distribution [15]. Notably, in most EI systems $D(x)$ is at least an order of magnitude smaller than $A(x)$. These raw projections are instrumental in the estimation of δ and β , which define the complex refractive index $\eta = 1 - \delta + i\beta$, with $\delta > 0$ [17]. In EI systems, the retrieved quantities are $I_\beta(x_s) := \int_{z_1}^{z_2} \beta(x_s, z) dz$ and $I_\delta(x_s) = \int_{z_1}^{z_2} \delta(x_s, z) dz$,

along with the scattering signal [15,18], which is not discussed in this article, where Mag is the magnification of the system and the variable $x_s = \frac{x}{Mag}$ denotes the demagnified transverse coordinate in the sample space. These line integrals are ideally extended over the region bounded by the axial coordinates of the M_1 (z_1) and the M_2 (z_2), by considering that $\beta(x_s, z)$ and $\delta(x_s, z)$ are approximately zero outside the sample. Here, $\beta(x_s, z)$ and $\delta(x_s, z)$ represent the distributions of β and δ , respectively, within the plane parallel to the axial direction and containing to the detector row of pixels being analyzed. $I_\beta(x_s)$ and $I_\delta(x_s)$ are derived from the transmittance $T(x_s) \approx e^{-2k_0 I_\beta(x_s)}$ and the illumination curve shift measured at the detector $\Delta_t^d = z_{od} \frac{\partial}{\partial x_s} I_\delta(x_s)$ [16,18], respectively, k_0 is the average wavenumber of the source spectrum and z_{od} is the distance from the sample to the detector. Assuming that the illumination curve variable t is sampled at M_1 , the shift Δ_t^d is demagnified [19], resulting in $B_S(x) - B_F(x) = B_S(Mag x_s) - B_F(Mag x_s) = \frac{\Delta_t^d}{Mag} = \frac{z_{od}}{Mag} \frac{\partial}{\partial x_s} I_\delta(x_s)$. It is important to note that these definitions are approximations rather than exact representations, as they neglect the effects of the source's polychromaticity by substituting it with the averaged wavenumber of the spectrum. This approximation is necessary because quantitative phase imaging systems cannot be accurately described using the concept of effective energy, as shown by Munro and Olivo [20]. $T(x)$ is estimated as the ratio of the intensity reaching the detector pixel x for the sample and flat projections. This is calculated by averaging the projections over the illumination curve, expressed as $T(x) = \frac{\int_{-\infty}^{\infty} (P_S^0(x,t) - D_S(x)) dt}{\int_{-\infty}^{\infty} (P_F^0(x,t) - D_F(x)) dt} = \frac{\sqrt{2\pi} A_S(x) C_S(x)}{\sqrt{2\pi} A_F(x) C_F(x)}$, where the offsets $D_S(x)$ and $D_F(x)$ have been removed, as they are considered negligible.

Then, the information about β and δ at the M_1 space can be retrieved as follows:

$$I_\beta(x_s) = -\frac{1}{2k_0} \log \left(\frac{A_S(Mag x_s) C_S(Mag x_s)}{A_F(Mag x_s) C_F(Mag x_s)} \right) \quad (2a)$$

$$I_\delta(x_s) = \frac{Mag}{z_{od}} \int_{-\infty}^{x_s} \left(B_S(Mag x'_s) - B_F(Mag x'_s) \right) dx'_s \quad (2b)$$

The final distributions $\beta(x_s, z)$ and $\delta(x_s, z)$ are obtained by applying the inverse Radon transform to Eq. (2a) and Eq. (2b), respectively, after acquiring multiple measurements at different rotation angles applied to the sample, usually covering a full 360-degree range.

3. Fast-Fourier transform based deconvolution

In this section, we describe the deconvolution algorithm we applied to the EI images, which is a standard Fourier transform based deconvolution algorithm, with additional precautions to ensure robustness and mitigate noise amplification during deconvolution.

Let $G(x) := \frac{1}{\sigma\sqrt{\pi}} e^{-\frac{x^2}{\sigma^2}}$ represent the point spread function (PSF) of the detector as a function of the spatial coordinate x . The raw projections, accounting for the XT effect, are given by:

$$P_F(x, t) = P_F^0(x, t) * G(x) \quad (3a)$$

$$P_S(x, t) = P_S^0(x, t) * G(x) \quad (3b)$$

where the symbol $*$ denotes the convolution operator.

In Fig. 1 we present examples of the retrieved refraction for different PSF widths, where σ is the standard deviation of $G(x)$. The simulations were performed using the EI simulator developed by Vittoria *et al.* [21]. We performed a monochromatic simulation at 21 keV with an extended source modeled as a Gaussian profile with Full Width at Half Maximum (FWHM) of the focal spot of $70\mu\text{m}$. Four points were sampled along the simulated illumination curve, corresponding to 18%, 57%, 100% and 38% of its maximum. The source to M_2 and source to M_1 distances were set to 0.87 m and 0.68 m, respectively, resulting in $Mag \approx 1.28$. The aperture sizes of M_1 and

M_2 were set as $10\mu\text{m}$ and $17\mu\text{m}$, respectively. To simulate a skipped detector mask, every other pixel was obscured, meaning only alternating pixels were active. Apart from the PSF standard deviation σ , these simulation parameters match those used for acquiring x-ray projections of the plastic rod sample described in section (5.1). In particular, the plot shows the term $B_S(x) - B_F(x)$ before integration. It is evident that the convolution acts as a smoothing function on the retrieved refraction as a function of the pixel row x . From Eqs. (3) we can derive explicitly $P_S^0(t; x)$ and $P_F^0(t; x)$ using the Fourier transform:

$$\mathcal{F}\{P_F^0(x, t)\}(v) = \frac{\mathcal{F}\{P_F(x, t)\}(v)}{\mathcal{F}\{G(x)\}(v)} \implies P_F^0(x, t)(v) = \mathcal{F}^{-1}\left\{\frac{\mathcal{F}\{P_F(x, t)\}(v)}{\mathcal{F}\{G(x)\}(v)}\right\} \quad (4a)$$

$$\mathcal{F}\{P_S^0(x, t)\}(v) = \frac{\mathcal{F}\{P_S(x, t)\}(v)}{\mathcal{F}\{G(x)\}(v)} \implies P_S^0(x, t)(v) = \mathcal{F}^{-1}\left\{\frac{\mathcal{F}\{P_S(x, t)\}(v)}{\mathcal{F}\{G(x)\}(v)}\right\} \quad (4b)$$

where $\mathcal{F}\{f(x)\}(v) = \int_{\mathbb{R}} f(x)e^{-i2\pi xv} dx$ is the Fourier transform of the function $f(x)$ evaluated at frequency v . Using the right-hand side of equations Eq. (4a) and Eq. (4b) we obtain simple analytical solutions to remove the XT. However, as the denominator terms $\mathcal{F}\{G(x)\}(v)$ approach zero for $|v| \gg 1$, the results can become highly noisy and ultimately impractical. To address this issue, we introduced a filter to reduce the noise in the signal:

$$P^0(x, t) = \mathcal{F}^{-1}\left\{\frac{\mathcal{F}\{P(x, t)\}(v)}{\mathcal{F}\{G(x)\}(v)} \chi(|v| \leq M) + \tau \mathcal{F}\{P(x, t)\} \chi(|v| > M)\right\}(x) \quad (5)$$

where the parameter τ is a constant introduced to ensure continuity in the spectral function within the inverse Fourier transform operator in Eq. (5). This prevents abrupt transitions that could otherwise introduce ringing artifacts in the spatial domain after applying $\mathcal{F}^{-1}\{\cdot\}$. The constant M represents the upper bound of the frequencies involved in the deconvolution. The symbol $\chi(\cdot)$ is the Heaviside function.

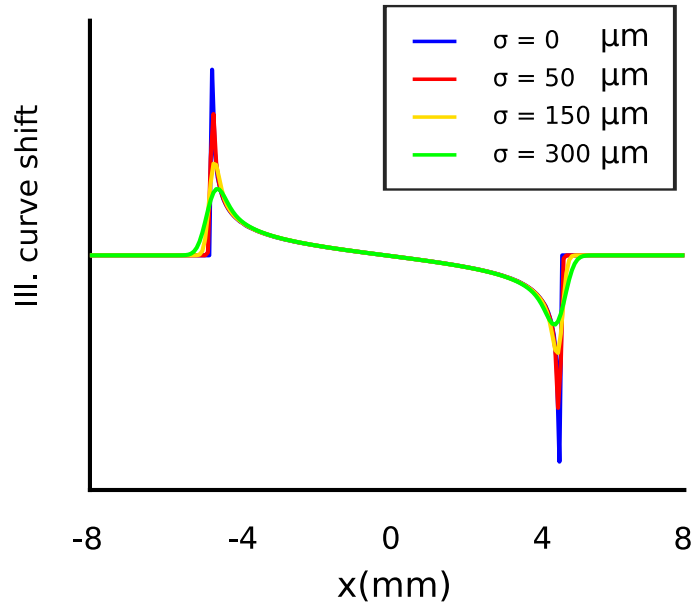


Fig. 1. Example of four simulated refraction signals with PSFs having different standard deviations σ .

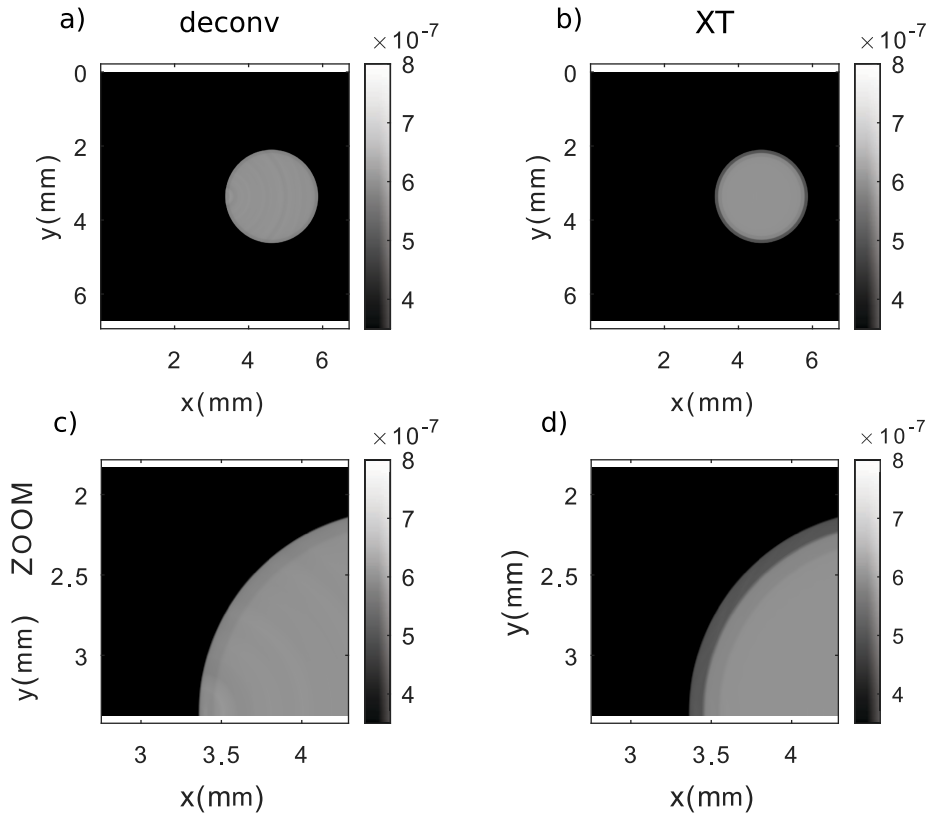


Fig. 2. Comparison of CT reconstructions of a simulated plastic cylinder: the plots a) and c) show results with the deconvolution algorithm applied, while plots b) and d) show results without deconvolution. The bottom plots provide zoomed-in views of the corresponding top plots, focusing on a region at the cylinder's edge.

On the one hand, the introduction of the filter reduces noise; on the other hand, it limits the range of the spectrum actively contributing to the deconvolution, leading to a loss of accuracy. A larger M allows for improved deconvolution procedure and also amplifies noise, indicating the need for a trade-off between noise amplification and deconvolution effectiveness. Through heuristic analysis, we found that setting M equal to 30% of the maximum magnitude of the spectrum's Fourier transform effectively prevents noise amplification. However, this approach results in a weakened deconvolution, as we will show in section (4.2). Once both the flat and sample projections have been deconvolved using Eq. (5), they can be fitted with Gaussian functions to retrieve the terms A , B , C and D , which will be used in the retrieval process described in Eqs. (2).

It should be noted that the application of the PSF to the projections in Eq. (1) has non-linear effects on all the terms A , B , C and D , which make the deconvolution a non commutative operator in this instance. A common erroneous practice is to deconvolve only the sample projections, assuming that the flat field is constant. However, this is not accurate, as there are significant variations in P_F^0 as a function of x , making this assumption imprecise as well. In Fig. 2 we show the slice corresponding to projections of a plastic cylinder, simulated using a Fourier optics-based approach developed by Vittoria *et al.* [21], where the sample is characterized by a certain spatial distribution of δ and β . For this simulation, we set $\delta = 6 \times 10^{-7}$ and $\beta = 3 \times 10^{-10}$. Figure 3(a) shows the values of δ resulting from the CT reconstructions for the central horizontal row of

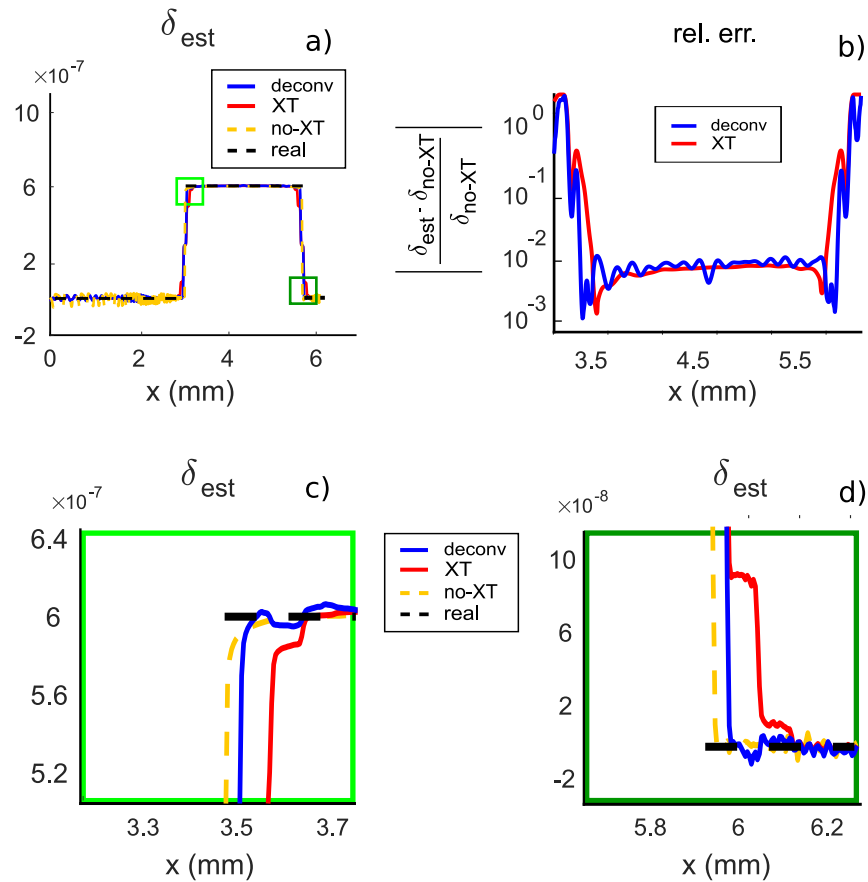


Fig. 3. a) Plot of the central horizontal line of pixels extracted from the simulated slices shown in Fig. 2. b) Relative error versus the δ values estimated without XT, plotted on a log scale for better readability. c) Zoom-in on the light-green box in a). d) Zoom-in on the dark-green box in a).

pixels extracted from the cylinder shown in Fig. 2, for four different representations of the same sample. The black dashed line represents the ground truth δ , referred to as the "real" value, which was used as input for the simulation. The yellow line shows the CT reconstruction when no XT was introduced in the simulation, labeled as "no-XT." The red line represents the simulation in which XT was introduced via convolution with a Gaussian-shaped PSF. The distances between the source and M_1 and source and M_2 , the energy level and the illumination curve were set according to the simulation described in Fig. 1. To enhance image details, 16 dithering steps were applied. The PSF standard deviation σ was set to $100 \mu\text{m}$. This larger σ was intentionally chosen to evaluate the algorithm under increased crosstalk conditions and corresponds to the distance between two adjacent apertures in a skipped-mask setup with a pixel size of $50 \mu\text{m}$. This case is labeled as "XT" in Fig. 3. The blue line represents the CT reconstruction of the simulation with XT, where the XT was then removed using a deconvolution algorithm; this case is labeled "deconv." In Fig. 3(b), the relative errors are plotted for the "XT" and "deconv" cases compared to the "no-XT" case, represented by the red and blue lines, respectively, on a logarithmic scale. To smooth the lines and improve the readability of the plot, a moving average of 10 pixels in the x -direction was applied. Additionally, only the region surrounding the simulated cylinder

is shown. The relative error in the "XT" case is notably higher at the edges of the cylinder, corresponding to pixels near 3.3 mm and 5.8 mm on the x-axis, ranging from approximately twice to an order of magnitude greater than that of the "deconv" case. This improved performance of the "deconv" case is further illustrated in Fig. 3(c) and Fig. 3(d), which provide zoomed-in views of the light green and dark green boxes in Fig. 3(a), respectively. In both zoomed-in plots, the "deconv" case remains closer to the "no-XT" case than the "XT" case, albeit with some perturbations introduced by the deconvolution algorithm.

As can be expected, this behavior indicates that XT causes blurring in the CT reconstructions, even when skipped masks are used. This will be further analyzed in the following sections.

The practical and efficient implementation of the deconvolution approach described above is performed by using the Fast-Fourier transform (FFT). From now on, we will describe this deconvolution approach as FFT-deconvolution.

4. Circulant matrix deconvolution

In this section, we demonstrate that applying projection deconvolution to a small number of pixels in each row improves the algorithm's robustness and reduces its susceptibility to noise. To explain this method, we represent the signals in their real, discrete form, as arrays of numbers where each value corresponds to the number of photons recorded by each pixel. In particular, the discrete version of Eqs. (1), are:

$$P_F^0[i, j] = A_F[i] e^{-\frac{(i[j]-B_F[i])^2}{2C_F[i]^2}} + D_F[i] \quad (6a)$$

$$P_S^0[i, j] = A_S[i] e^{-\frac{(i[j]-B_S[i])^2}{2C_S[i]^2}} + D_S[i] \quad (6b)$$

where i and j are indices representing the pixel position and the points acquired along the illumination curve, respectively. The discrete version of the convolution described in Eqs. (3) can be expressed as a multiplication with a circulant matrix \mathcal{M}_G , as:

$$P_F[i, j] = \sum_{k=1}^N \mathcal{M}_G[i, k] \cdot P_F^0[k, j] \quad (7a)$$

$$P_S[i, j] = \sum_{k=1}^N \mathcal{M}_G[i, k] \cdot P_S^0[k, j] \quad (7b)$$

where \mathcal{M}_G is the following circulant matrix [22]:

$$\mathcal{M}_G = \begin{bmatrix} G(0) & G(\Delta) & G(2\Delta) & \cdots & G((N-1)\Delta) \\ G(\Delta) & G(0) & G(\Delta) & \cdots & G((N-2)\Delta) \\ G(2\Delta) & G(\Delta) & G(0) & \cdots & G((N-3)\Delta) \\ \vdots & \vdots & \vdots & \ddots & \vdots \\ G((N-1)\Delta) & G((N-2)\Delta) & G((N-3)\Delta) & \cdots & G(0) \end{bmatrix} \quad (8)$$

where N is the number of pixel in a row that are used to compute the deconvolution, Δ is the detector pixel size and the terms $G(n\Delta)$ represent the PSF evaluated at the x coordinate corresponding to the width of the n -th adjacent pixels in a row of the detector.

The deconvolution process is equivalent to inverting \mathcal{M}_G and multiplying \mathcal{M}_G^{-1} by the projections. Since \mathcal{M}_G is a circulant matrix, it can be efficiently inverted using the Discrete Fourier Transform (DFT) matrix, a fundamental tool in signal processing, defined as:

$$Q = \frac{1}{\sqrt{N}} \begin{bmatrix} 1 & 1 & 1 & \dots & 1 \\ 1 & \omega & \omega^2 & \dots & \omega^{N-1} \\ 1 & \omega^2 & \omega^4 & \dots & \omega^{2(N-1)} \\ \vdots & \vdots & \vdots & \ddots & \vdots \\ 1 & \omega^{N-1} & \omega^{2(N-1)} & \dots & \omega^{(N-1)(N-1)} \end{bmatrix} \quad (9)$$

where $N \times N$ is the size of the matrix, and $\omega = e^{-2\pi i/N}$ is the complex N -th root of unity.

4.1. Inversion in the Fourier domain

The matrix inversion is computed in the Fourier domain:

$$D = Q \cdot \mathcal{M}_G \cdot Q^\dagger, \quad (10)$$

where the symbols \cdot and \dagger represent the matrix product and the conjugate transpose operator, respectively. It can be observed that the matrix D is diagonal in the Fourier domain [22]. Consequently, the inverse of \mathcal{M}_G is given by:

$$\mathcal{M}_G^{-1} = Q^\dagger \cdot D^{-1} \cdot Q, \quad (11)$$

where D^{-1} is easily computed by inverting each diagonal element of the matrix D . Using this, the XT-removed projection $P^0[i, j]$, is obtained as:

$$P_F^0[i, j] = \sum_{k=1}^N \mathcal{M}_G^{-1}[i, k] P_F[k, j] \quad (12a)$$

$$P_S^0[i, j] = \sum_{k=1}^N \mathcal{M}_G^{-1}[i, k] P_S[k, j] \quad (12b)$$

When applied to all pixels in a detector row, the discrete solution provided above (FFT-deconvolution) suffers from the same noise-sensitivity issues described in section (3), which in that case have been reduced by filtering the spectrum with Eq. (5). In the next section, we explain how the circulant-matrix deconvolution approach (CM) can be made more robust by dividing the projections into smaller segments, processing each segment independently, then recombining them to reconstruct the entire deconvolved row of pixels. This iterative process is applied across the entire detector, enabling the sampling of the function $G(x)$ only in regions where its magnitude is sufficiently large. This approach reduces the impact of noise on the deconvolution while preserving high-frequency information, which would otherwise be lost when using the filter described in Eq. (5).

4.2. Efficient implementation of the circulant matrix-based deconvolution

The described approach is highly effective for deblurring images when the blur kernel is known or can be accurately estimated, in which case it is particularly well-suited for applications in optical and medical imaging, where high-fidelity image restoration is crucial. As mentioned in the previous section, to enhance the robustness of the deconvolution, it is preferable to apply the algorithm to smaller sections of pixels rather than to the entire row at once.

Let N_x represent the total number of pixels in each row of the detector. The algorithm begins by evaluating Eq. (8), Eq. (9), Eq. (10) and Eq. (11) for a section of N pixels (with $N < N_x$). Within this section, a smaller window of N_w pixels, centered within the N pixels, is selected for the deconvolution. The process is then iterated while shifting by N_w pixels at each step, until the entire row is covered (N_x pixels). To enhance the robustness of the deconvolution, the entire process is repeated three times with different values of N_w and N , and the results for each pixel are averaged. We set three values for N , denoted as N_1, N_2 and N_3 , respectively. Similarly, we defined three values for N_w , denoted as N_{w1}, N_{w2} and N_{w3} . We have observed heuristically that setting the section length $N \approx 35$ and window length $N_w \approx 25$, results in high-quality deconvolution. Based on multiple tests, we suggest using these values, as they remain consistent when the PSF width σ is less than twice the pixel size. However, for larger values of σ , larger N and N_w values may be required to ensure accurate deconvolution. Building on this observation, we chose the parameters for the three iterations to remain close to these values while ensuring distinct step sizes. Specifically, we configured the CM-deconvolution scheme with parameters $[N_1, N_2, N_3] = [32, 34, 36]$ and $[N_{w1}, N_{w2}, N_{w3}] = [25, 27, 28]$. Below we provide the pseudo-code illustrating this process, where the term $[1 : N]$ represents the array of indices from 1 to N (included), and $\text{zeros}(\text{size}(P))$ refers to a null matrix with the same dimensions as the matrix P :

Pseudo-code CM deconvolution:

1. Initialization of $P^0 = \text{zeros}(\text{size}(P))$
2. For i from 1 to 3 (three repetitions for robustness):
 - (a) Initialization of the the temporary deconvolved projection for the i -th repetition:
 $P_r^0 = \text{zeros}(\text{size}(P))$;
 - (b) Update of the pixels segment length: $N = N_i$
 - (c) Update of the internal pixel segment length: $N_w = N_{w_i}$
 - (d) Computation of the circulant matrix \mathcal{M}_G from $G(x)$ of dimension $N \times N$
 - (e) Computation of DFT matrix Q of dimension $N \times N$
 - (f) Computation of the diagonal matrix $D = Q \cdot \mathcal{M}_G \cdot Q^\dagger$,
 - (g) Computation of the inverse matrix $D^{-1}(h, k) = \frac{1}{D(h, k)}$, if $h = k$, 0 otherwise
 - (h) Computation of the inverse matrix $\mathcal{M}_G^{-1} = Q^\dagger \cdot D^{-1} \cdot Q$
 - (i) Computation of the number of segments for i -th: $N_{seg} = \left\lfloor \frac{N_x - N}{N_w} \right\rfloor + 1$
 - (j) First index of the internal segment of pixels: $i_{w_0} = \left\lfloor \frac{N - N_w}{2} \right\rfloor$
 - (k) Local indices of the internal segment of pixels within the current segment of pixels:
 $I_w = i_{w_0} + [1 : N_w]$;
 - (l) For i_s from 1 to N_{seg} :
 - i. Extraction of the i_s^{th} segment indices $I_s = [1 : N] + (i_s - 1)N_w$;
 - ii. Extraction of the i_s^{th} local indices: $I_{w_s} = I_w + (i_s - 1)N_w$;
 - iii. Computation of the deconvolved segment: $P_{tmp} = \mathcal{M}_G^{-1} \cdot P_s[I_s, j]$
 - iv. Update the deconvolved projection $P_r^0[I_{w_s}, j] = P_{tmp}[I_w]$
 - (m) Accumulate result across repetitions: $P^0 \leftarrow P^0 + P_r^0$
- (3) Average results: $P^0 \leftarrow \frac{P^0}{3}$

A visual representation of the index arrangement corresponding to the pseudo-code described above is shown in Fig. 4.

It is worth noting that the same procedure described above using CM could have been performed by applying Fast Fourier Transforms (FFT) to the row sections of pixels. However, although the computation of the Fourier transform is generally considerably faster when using the FFT algorithm compared to CM, this is not the case in low-dimensional scenarios, such as the one discussed here, where the DFT matrix dimension is approximately 30×30 . In this situation, we have heuristically observed that the computation is around two times faster with CM compared to FFT.

To highlight the differences between the CM-deconvolution algorithm described above and the FFT-deconvolution algorithm of Eq. (5), Fig. 5 compares the performance of the two algorithms

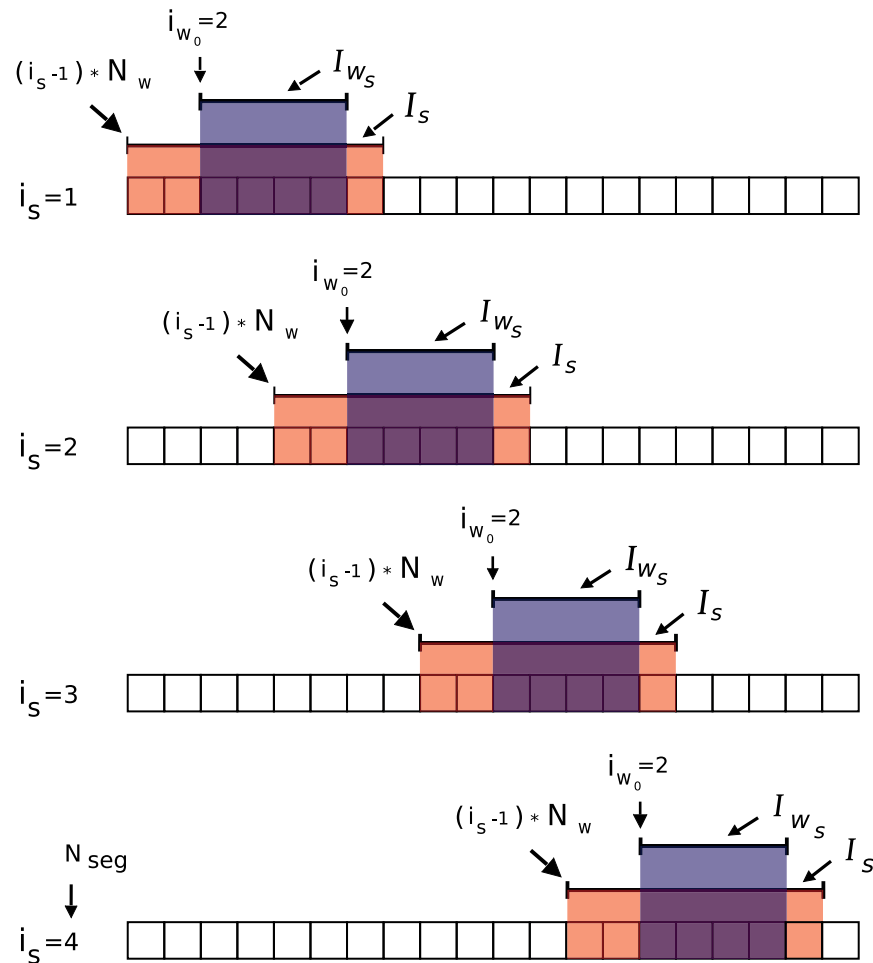


Fig. 4. Schematic representation of the index arrangement in the CM-deconvolution algorithm for a single repetition, with $N_x = 20$, $N = 7$, and $N_w = 4$. Under these parameter settings, $i_{w_0} = 2$, and the algorithm performs $N_{seg} = 4$ iterations in total. In each iteration i_s , the red-shaded region represents the segment of indices I_S , while the blue-shaded region corresponds to the local segment of indices I_{W_S} . The deconvolution is applied over I_S , but only the pixels within I_{W_S} are stored. In this configuration, the first two and last two pixels of the output are not updated by the deconvolution algorithm and they are set to zero.

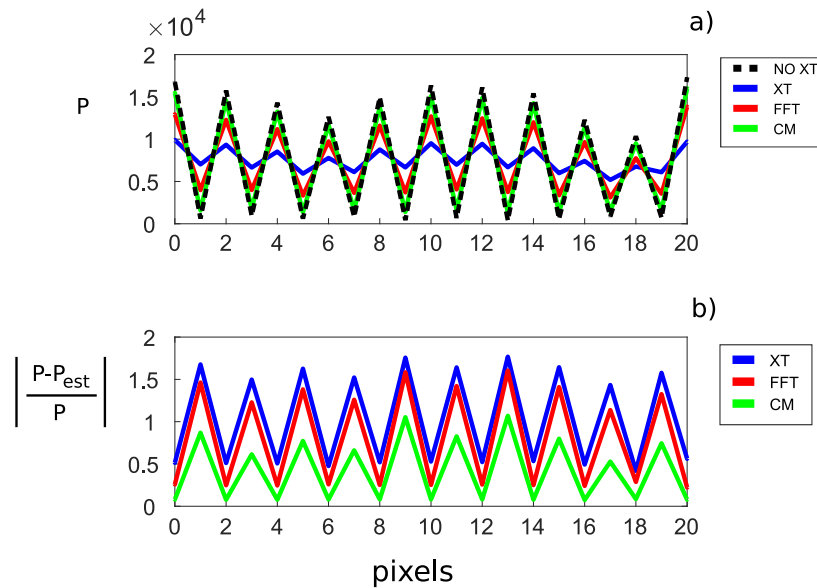


Fig. 5. a) Raw projections of simulations without XT, with XT removed with the FFT-deconvolution and XT removed with CM approach. b) Relative error of the three approaches versus the ideal non-XT case.

on the same sample used in Fig. 3. However, instead of presenting the retrieved refraction, this comparison focuses on the raw projections, inclusive of the detector columns "obscured" by the skipped mask.

From Fig. 5(a), it can be observed that the CM-deconvolution results align more closely with the ideal case in which XT was not included in the simulations compared to the FFT-deconvolution. The relative error of the uncorrected XT case and the FFT and CM deconvolution algorithms versus the ideal "non-XT" case are shown in Fig. 5(b).

Although the CM algorithm produces a reduced error compared to the other methods, the error remains high for the obscured pixels. However, this is not problematic, as these pixels correspond to the skipped regions, where the projection values are nearly zero and which are ultimately removed from the images. As a result, an error of 50% in these pixels is negligible compared to the signal from the open pixels.

5. Experimental data analysis

In this section, we analyze two experimental datasets acquired at the Advanced X-Ray Imaging (AXIm) Labs at University College London. Each acquisition involved 8 dithering steps. The source-to- M_1 distance, source-to- M_2 distance and aperture sizes of M_1 and M_2 were set as the simulations described in Fig. 1. All samples were placed within a plastic container with a diameter of 1.6 cm and a height of 5 cm, corresponding to the largest annular region shown in all figures in the next section.

We used a Hamamatsu CMOS Flat Panel Sensor (C9732DK) with a $50\mu\text{m}$ pixel size and direct deposition CsI scintillator. The source was a Rigaku MicroMax-007HF with Molybdenum Anode and approximately $70\mu\text{m} \times 100\mu\text{m}$ focal spot. The PSF was estimated as spilling $\sim 40\%$, $\sim 12\%$, $\sim 2\%$ signal to the first, second and third adjacent pixels, respectively.

5.1. Analysis on a plastic rod sample

We applied the presented deconvolution algorithms to a CT acquisition of a polyethylene rod with a diameter of 6.6 mm and a height of 4 cm. The illumination curve for this experimental data was set to match the simulation described in Fig. 1. 720 projections were acquired at equally spaced angles over a 360-degree range. Plots a) and c) in Fig. 6 show the reconstructed distributions of δ and β for the central slice of the cylinder in the $z-x$ plane, deconvolved using the CM method. It can be noted that β -map is noisier than the corresponding δ -map, likely due to the lower signal intensity of the former. To evaluate the deconvolution performance, we reconstructed the distributions of δ and β for the XT-affected case, CM deconvolved case (see Supplement 1 for analogous images generated using a deconvolution algorithm based on a deep learning model (see Fig. (S2)). From each reconstruction, we extracted 100 segments of 41 pixels each for further analysis. These linear segments were centered on the edge circumference of the plastic rod, with their radial orientations spanning the entire circle. In particular, the 100 segments correspond to 100 angles evenly distributed over 2π . An example of a single directional segment is illustrated by the two red lines crossing the rod in images a) and c). Since the plastic cylinder has a homogeneous refractive index and is surrounded by air, each segment is expected to result in a step-like line, approximately equal to zero in the regions corresponding to air. In plots b) and d), we show the average of all of these segments for the δ and β , respectively. It is evident that the XT-affected reconstructions appears smoothed at the edges, consistently with the simulations shown in Fig. 1 and Fig. 2. In contrast, the deconvolved cases successfully restore the expected sharp edge profile.

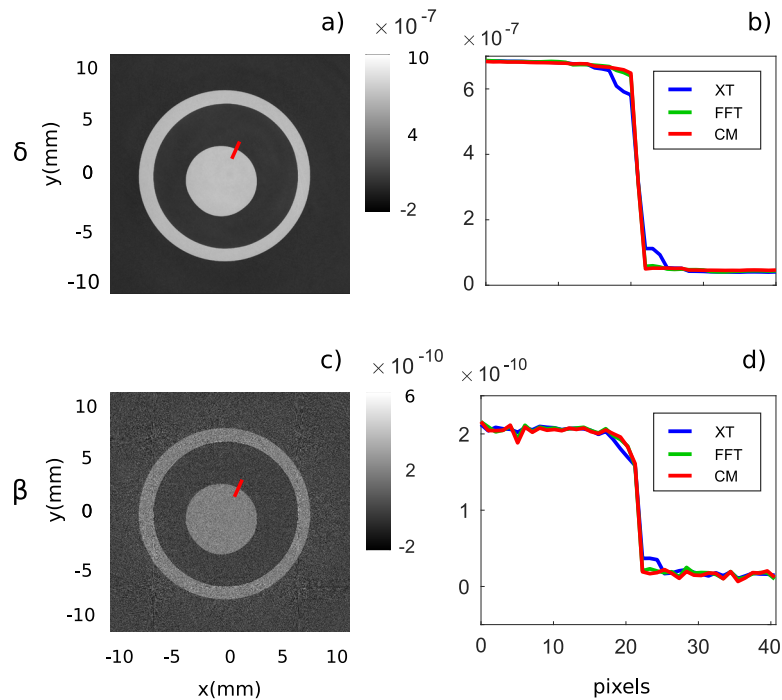


Fig. 6. a) and c) δ -map and β -map slices of the CM-deconvolved projections, respectively. b) and d) line plots corresponding to the average of 100 segments of 41 pixels crossing the edge between the plastic cylinder and air, for the XT-affected, FFT-deconvolved and CM-deconvolved cases, respectively.

5.2. Analysis of a post-mortem mouse skull sample

This section analyzes XT-affected and deconvolved CT acquisitions of a sample featuring a mouse skull containing the intact brain. For this experiment, five points were used along the illumination curve, corresponding to 14%, 58%, 100%, 58% and 14% of its maximum. For the mouse sample, 2000 projections were acquired at equally spaced angles over a 360-degree range. The tissue sample was provided by the Pauws lab as part of a UK Home Office Project License (number: PP8161503) under the UK Animals (Scientific Procedures) Act 1986. The animal procedure complied with the ARRIVE guidelines and was performed under the supervision of UCL Biological Services. The specimen is a postnatal day 21 (P21) wild-type (CD-1 strain) mouse. Figure 7 shows reconstructed δ -map slice for an intact mouse skull. The green region highlights the edge of the container, where the XT effect is most apparent. The green region is zoomed in images b) and c), corresponding to the XT-affected and CM cases, respectively, demonstrating that CM deconvolution effectively eliminate the XT artifact. Please refer to [Supplement 1](#) for analogous images generated using a deep learning-based deconvolution algorithm (see Fig. (S3) and Fig. (S4)), along with additional δ -map slices for a mouse skull without the brain. We analyzed a region containing detailed structures of the skull and brain. While the results for this sample suggests that the CM-deconvolution method is robust in dealing with noise, further investigations would be needed for a more comprehensive noise assessment.

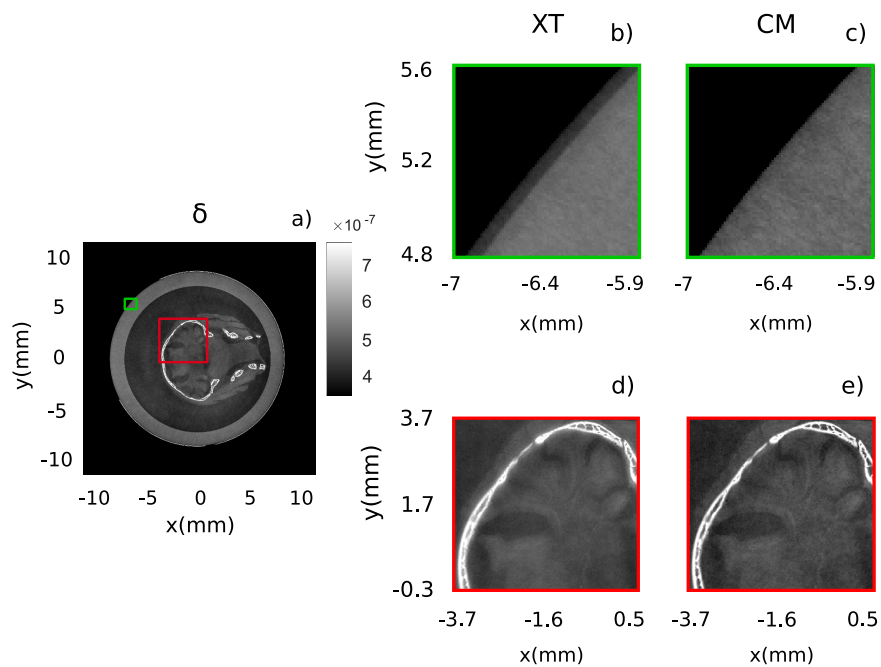


Fig. 7. δ -map of a mouse skull containing the intact brain, from XT-affected data and data deconvolved with the CM method.

Remarkably, to the best of our knowledge, this is the first instance of a soft-tissue details in a murine brain being observed in a laboratory-based phase contrast CT reconstruction of an intact skull. This region, highlighted by a red box, is zoomed in images d), and e), corresponding to the XT-affected, and CM cases, respectively. To compare the performance of the deconvolution approaches also on a specimen with higher inherent contrast, we also scanned a mouse skull from which the brain had been removed. Results are presented in [Supplement 1](#).

5.3. Computational time

In this section we discuss the computational time related to compute the CT-reconstruction of the mouse sample described in section (5.2). We compare the reconstruction without deconvolution correction to those using the two deconvolution methods introduced in this article: FFT-deconvolution and CM-deconvolution. All computations were carried out using a computer with an NVIDIA A6000 48GB GPU, and two CPU AMD EPYC 7453 with 28-Cores. Both the FFT-deconvolution and the CM-deconvolution employed a vectorized implementation in MATLAB (Matlab R2021b), run on the system's CPUs.

The computational time to retrieve the information about δ and β using Eqs. (2), which are common to all methods, involves Gaussian fitting of the illumination curve for all detector pixels across 2,000 acquisition angles and 8 dithering steps, taking approximately 4 hours. CT reconstructions were performed using the MATLAB ASTRA Toolbox with the Feldkamp-Davis-Kress (FDK) algorithm executed on the GPU. The deconvolution of raw projections using FFT-deconvolution and CM-deconvolution took approximately 24 minutes and 52 minutes, respectively. CM-deconvolution is slower than FFT-deconvolution because it involves three repetitions and operates on scanned sections rather than entire rows of pixels, leading to a considerable increase in the computational load. Notably, the average computation time for each repetition is approximately 17 minutes and 20 seconds. This means that, without averaging, CM-deconvolution would actually be faster than FFT-deconvolution. Performing the CM-deconvolution with the three repetitions adds approximately 20% to the total computation time of the CT reconstruction without deconvolution.

6. Conclusion

In this study, we addressed the challenge of crosstalk (XT) in x-ray phase contrast imaging (XPCI) systems utilizing the edge illumination (EI) technique. Despite significant advancements in EI, XT remains a critical issue that reduces the accuracy and clarity of reconstructed images, particularly at interfaces and fine structures, where the benefits of phase contrast are greatest. By analyzing the limitations of existing approaches and introducing appropriate deconvolution methods, we have provided a robust solution to mitigate XT effects.

Initially, we demonstrated that XT persists even in state-of-the-art EI systems with skipped masks, leading to blurring and quantitative inaccuracies in the retrieved phase and attenuation signals. A detailed mathematical model was used to illustrate the non-linear effects of XT on projection data and its influence on image reconstruction. The convolution-based nature of XT was systematically analyzed, revealing that both sample and flat projections must be deconvolved to achieve accurate retrieval. We presented a FFT-based deconvolution algorithm accompanied by an equivalent but more robust version that makes use of circulant matrices (CM). The FFT-deconvolution utilized spectral filtering to mitigate noise amplification, while the CM method leveraged linear algebra techniques for enhanced stability and precision.

Validations using simulated and experimental data, the latter involving a polyethylene rod phantom and a mouse skull with the intact brain, demonstrated the effectiveness of the proposed methods. CM-based deconvolutions significantly reduced XT artifacts, restoring edge sharpness and improving contrast without introducing additional noise. In what is to the best of our knowledge the first time, details of the soft tissue in a mouse brain were visualized in a laboratory-based phase-contrast CT reconstruction of an intact skull. While soft tissues are visible also in XT-affected reconstruction, their visibility is improved in CM corrected ones. Our results confirm that the CM method is highly effective in addressing XT with acceptable computational overheads. This technique is robust and applicable to diverse experimental setups, making it a valuable tool for enhancing XPCI imaging quality.

Funding. Engineering and Physical Sciences Research Council (EP/X018377/1, EP/W008092/1, EP/R513143/1–2592407, EP/T517793/1–2592407); Royal Academy of Engineering (CiET1819/2/78).

Acknowledgment. This work was supported by the Engineering and Physical Sciences Research Council (EPSRC - Grant EP/X018377/1). MM and MD were also supported by EPSRC (EP/W008092/1; EP/R513143/1–2592407 and EP/T517793/1–2592407). AO is supported by the Royal Academy of Engineering under their Chair in Emerging Technologies scheme (CiET1819/2/78).

Disclosures. The authors declare no conflicts of interest.

Data availability. Data underlying the results presented in this paper are not publicly available at this time but may be obtained from the authors upon reasonable request.

Supplemental document. See [Supplement 1](#) for supporting content.

References

1. A. Olivo, K. Ignatyev, P. R. Munro, *et al.*, “Design and realization of a coded-aperture based X-ray phase contrast imaging for homeland security applications,” *Nucl. Instruments Methods Phys. Res. Sect. A: Accel. Spectrometers, Detect. Assoc. Equip.* **610**(2), 604–614 (2009).
2. A. Olivo, S. Gkoumas, M. Endrizzi, *et al.*, “Low-dose phase contrast mammography with conventional x-ray sources,” *Med. Phys.* **40**(9), 090701 (2013).
3. L. Massimi, T. Suaris, C. K. Hagen, *et al.*, “Volumetric High-Resolution X-Ray Phase-Contrast Virtual Histology of Breast Specimens With a Compact Laboratory System,” *IEEE Trans. Med. Imaging* **41**(5), 1188–1195 (2022).
4. F. Arfelli, M. Assante, V. Bonvicini, *et al.*, “Low-dose phase contrast x-ray medical imaging,” *Phys. Med. Biol.* **43**(10), 2845–2852 (1998).
5. R. A. Lewis, “Medical phase contrast x-ray imaging: Current status and future prospects,” *Phys. Med. Biol.* **49**(16), 3573–3583 (2004).
6. T. Donath, F. Pfeiffer, O. Bunk, *et al.*, “Toward clinical X-ray phase-contrast CT: Demonstration of enhanced soft-tissue contrast in human specimen,” *Invest. Radiol.* **45**(7), 445–452 (2010).
7. S. C. Mayo, A. W. Stevenson, and S. W. Wilkins, “In-Line Phase-Contrast X-ray Imaging and Tomography for Materials Science,” *Materials* **5**(5), 937–965 (2012).
8. A. Momose, T. Takeda, Y. Itai, *et al.*, “Phase-contrast X-ray computed tomography for observing biological soft tissues,” *Nat. Med.* **2**(4), 473–475 (1996).
9. F. Arfelli, G. Barbiellini, V. Bonvicini, *et al.*, “An Edge-On silicon strip detector for X-ray imaging,” *IEEE Trans. Nucl. Sci.* **44**(3), 874–880 (1997).
10. A. Olivo, “Edge-illumination x-ray phase-contrast imaging,” *J. Phys.: Condens. Matter* **33**(36), 363002 (2021).
11. G. Havariyou, L. Massimi, C. Hagen, *et al.*, “Modulation transfer function (MTF) evaluation for x-ray phase imaging system employing attenuation masks,” *Phys. Med. Biol.* **68**(9), 09NT02 (2023).
12. A. Olivo and R. D. Speller, “Deconvolution of x-ray phase contrast images as a way to retrieve phase information lost due to insufficient resolution,” *Phys. Med. Biol.* **54**(15), N347–N354 (2009).
13. A. Olivo and R. Speller, “Modelling of a novel x-ray phase contrast imaging technique based on coded apertures,” *Phys. Med. Biol.* **52**(22), 6555–6573 (2007).
14. K. Ignatyev, P. R. Munro, R. D. Speller, *et al.*, “Effects of signal diffusion on x-ray phase contrast images,” *Rev. Sci. Instrum.* **82**(7), 073702 (2011).
15. M. Endrizzi, P. C. Diemoz, T. P. Millard, *et al.*, “Hard X-ray dark-field imaging with incoherent sample illumination,” *Appl. Phys. Lett.* **104**(2), 024106 (2014).
16. L. Massimi, T. Partridge, A. Astolfo, *et al.*, “Optimization of multipoint phase retrieval in edge illumination X-ray imaging: A theoretical and experimental analysis,” *Med. Phys.* **48**(10), 5884–5896 (2021).
17. A. Olivo and E. Castelli, “X-ray phase contrast imaging: From synchrotrons to conventional sources,” *Rivista del Nuovo Cimento* **37** (2014).
18. F. A. Vittoria, M. Endrizzi, P. C. Diemoz, *et al.*, “X-ray absorption, phase and dark-field tomography through a beam tracking approach,” *Sci. Rep.* **5**(1), 16318 (2015).
19. P. R. Munro, C. K. Hagen, M. B. Szafraniec, *et al.*, “A simplified approach to quantitative coded aperture X-ray phase imaging,” *Opt. Express* **21**(9), 11187–11201 (2013).
20. P. R. Munro and A. Olivo, “X-ray phase-contrast imaging with polychromatic sources and the concept of effective energy,” *Phys. Rev. A* **87**(5), 053838 (2013).
21. F. A. Vittoria, P. C. Diemoz, M. Endrizzi, *et al.*, “Strategies for efficient and fast wave optics simulation of coded-Aperture and other x-ray phase-contrast imaging methods,” *Appl. Opt.* **52**(28), 6940 (2013).
22. P. C. Hansen, “Deconvolution and regularization with Toeplitz matrices,” *Numerical Algorithm* **29**(4), 323–378 (2002).